Bubble size distribution and electrode coverage at porous nickel electrodes in a novel 3-electrode flow-through cell

Rox, H.; Bashkatov, A.; Yang, X.; Loos, S.; Mutschke, G.; Gerbeth, G.; Eckert, K.;

Originally published:

November 2022

International Journal of Hydrogen Energy 48(2023)8, 2892-2905

DOI: https://doi.org/10.1016/j.ijhydene.2022.10.165

Perma-Link to Publication Repository of HZDR:

https://www.hzdr.de/publications/Publ-35344

Bubble size distribution and electrode coverage at porous nickel electrodes in a novel 3-electrode flow-through cell

Hannes Rox[a,*], Aleksandr Bashkatov[a,b,c], Xuegeng Yang[a], Stefan Loos[d], Gerd Mutschke[a], Gunter Gerbeth[a], Kerstin Eckert[a,b,c,*]

[a] *Institute of Fluid Dynamics, Helmholtz-Zentrum Dresden-Rossendorf, Bautzner Landstrasse 400, Dresden, 01328 Germany*
[b] *Hydrogen Lab, School of Engineering, Technische Universität Dresden, Dresden, 01062 Germany*
[c] *Institute of Process Engineering and Environmental Technology, Technische Universität Dresden, Dresden, 01062 Germany*
[d] *Fraunhofer Institute for Manufacturing Technology and Advanced Materials IFAM, Branch Lab Dresden, Winterbergstr. 28, 01277 Dresden, Germany*

Abstract

A novel 3-electrode cell type is introduced to run parametrical studies of H_2 evolution in an alkaline electrolyte on porous electrodes. Electrochemical methods combined with a high-speed optical measurement system are applied simultaneously to characterize the electrodes and the bubble dynamics in terms of bubble size distribution and coverage of the working electrode. Three different cathodes made of expanded nickel are investigated at applied current densities of $|j| = 10$ to $200\,\mathrm{mA\,cm^{-2}}$ without forced flow and at a flow rate of $5\,\mathrm{ml\,min^{-1}}$. The applied current density is found to significantly influence both the size of detached bubbles and the surface coverage of the working electrode. The forced flow through the cathodes is found to strongly reduce the bubble size up to current densities of about 100 mA $\mathrm{cm^{-2}}$, whereas the initial transient until the cathode surface is completely covered by bubbles is only marginally affected by the flow-through.

Keywords: bubble dynamics, alkaline electrolysis, porous electrodes, machine learning, additive manufacturing, membraneless electrolyzer

1. Introduction

Water electrolysis using solar- or wind-derived electricity to produce high-purity hydrogen gas is a promising pathway towards a net-zero-emissions industry [1, 2]. Hydrogen could replace the fossil fuels often used in industry [3] and be an alternative in applications that are hard to directly electrify, e.g., aviation, shipping and inter-seasonal energy storage, or used to produce synthetic

*Corresponding authors: h.rox@hzdr.de (Hannes Rox), k.eckert@hzdr.de (Kerstin Eckert)

natural gas and various synthetic liquid fuels and e-fuels [4]. Although today's production of pure hydrogen gas almost entirely relies on fossil fuels [2], the priority is to shift the existing hydrogen production sector toward renewable/green hydrogen using wind and solar energy [5, 6, 7]. Alkaline water electrolysis is still the most mature technology that requires only little of platinum-group metals, although suffering from lower efficiencies and current densities when compared to other technologies. One reason for this, among others, is that considerable losses are caused by the generated hydrogen and oxygen bubbles, which increase the ohmic contribution to the overall overpotential as they block the electrode surface and increase electrolyte resistance [8, 9, 10, 11]. To reduce energy losses and thus make green hydrogen cheaper, better knowledge of how to further advance the bubble departure is necessary.

Besides the operating expenditures (OPEX), which in the long term are mainly caused by the electricity consumption and lack of efficiency, capital expenditures (CAPEX) also need to be decreased [12]. One promising approach for a cheaper new cell design is so-called membraneless electrolyzers. In general there are three different types of membraneless electrolyzers: flow-through [13, 14, 15, 16, 17, 18], flow-by [19, 20, 21] and decoupled electrolyzers [22, 23, 24, 25, 26]. Here, we focus on flow-through electrolyzers, where the electrolyte flowing through porous electrodes is used to keep the products H_2 and O_2 separated by directly flushing them out of the cell in separate channels [13, 14, 15, 16, 17, 18]. The elimination of the membrane in flow-through electrolyzers both simplifies the overall design and improves the impurity tolerance, thus enabling the operation with tap water [12]. As a result, a significant reduction of the CAPEX and OPEX can be expected. Hence, with decreasing costs for electrical power, the produced hydrogen could become economically competitive [12].

The diameter of the bubbles d_B at the detachment and the coverage of the electrode A_{cov} by those bubbles are critical parameters for effectively separating the products using the electrolyte flow and for achieving satisfactory overall efficiency [8, 13, 17]. In membraneless water electrolyzers, the efficiency is already reduced by higher ohmic losses compared to zero-gap alkaline or polymer electrolyte membrane (PEM) electrolyzers [12]. Therefore, it is crucial to optimize the geometry and surface of the porous electrodes of the membraneless design. Gillespie et al. [13] performed a detailed study on the relation between the electrode gap, flow velocity and applied current density for a membraneless divergent-electrode-flow-through (DEFT) cell. Higher electrode coverage and the possible blocking of pores lead to higher losses due to the increasing pressure drop and the higher ohmic resistance. More importantly, bubbles at the inner site of each electrode can form a gas meniscus, resulting in the crossover of the products as soon as they overlap [13]. Similar effects of the electrode gap were reported by Pang et al. [19] and Rajaei et al. [27].

The electrogenerated gas bubbles growing at the electrodes experience a number of forces including electric, hydrodynamic, thermocapillary forces, and buoyancy [28, 29, 30, 31, 32, 33]. When the bubbles are surface attached, they experience additional contact pressure and surface tension forces that needs to

be further overcome prior to the bubble departure, leading to an increase in the overpotential [34]. Furthermore, bubble-bubble coalescence events are known to promote faster detachment, especially at a high current density j. However, the bubbles growing inside a porous electrode are generally more easily entrapped due to densely packed catalytic surface areas and weak convective flows.

In general, porous electrodes such as meshes or foams offer large areas for electrochemical reactions, and there are many cavities on the surface, e.g., in the weave knots of woven meshes. This leads to a higher number of nucleation sites compared to planar electrodes [35]. If the geometry or the surface of the electrodes are adjusted, the bubble dynamics can be improved such that smaller bubbles detach faster. In general, small pore sizes lead to a homogeneous flow distribution and a high reactive surface area [27]. However, the bubbles entrapped inside the electrode lead to an increase in the overpotential and in the pressure drop [34]. Lee et al. [36] performed a study on the structural effect of an electrode mesh. For the expanded meshes, it was proven that the overpotential decreases as the ratio of pore to strand width converges to 1. From this study it can be concluded that a hydrophilic surface will favor a re-wetting of the electrode and, by that means, remove gas bubbles with a smaller departure diameter and re-cover the active area. A similar influence of the mesh structure on the efficiency was also reported by Zhang et al. [34].

Structures incorporated into the porous electrode, such as tapered or expanding channels, can impose a capillary force which enhances the bubble detachment and the bubble transport inside the porous electrode [8, 37]. Another possibility is using different pore sizes in the inner and outer regions of a porous electrode. This can stimulate bubble coalescence and splitting processes in a targeted manner [38]. Besides the bubble detachment, the efficiency of the gas evolution has to be taken into account. This is affected by the competing processes of mass transfer to the liquid bulk and to the adhering bubbles [39]. The mass transfer is influenced by the bubble coverage, which moreover affects the actual current density [39, 40, 41, 42].

The present study uses a novel, 3D-printed membraneless electrolysis cell developed as a platform for analyzing the bubble dynamics and electrochemical performance of porous electrodes. By simultaneously characterizing the size of the detached bubbles, d_{B}, the electrode coverage A_{cov} and overpotential losses over a wide range of current densities j, it is shown that the current density influences both, d_{B} and A_{cov}, significantly. Additionally, the effect of the applied electrolyte flow through the porous electrode is studied. This new type of cell provides a reproducible and uniform way to jointly characterize both the electrochemical performance and the bubble dynamics in terms of bubble size distribution and electrode coverage for different electrode geometries, materials or coatings over a wide range of parameters. Thus, the new cell has the potential to become a valuable tool in the simultaneous optimization of the electrochemical properties and the resulting bubble dynamics of new electrode materials, geometries and coatings.

2. Materials and Methods

2.1. Cell design

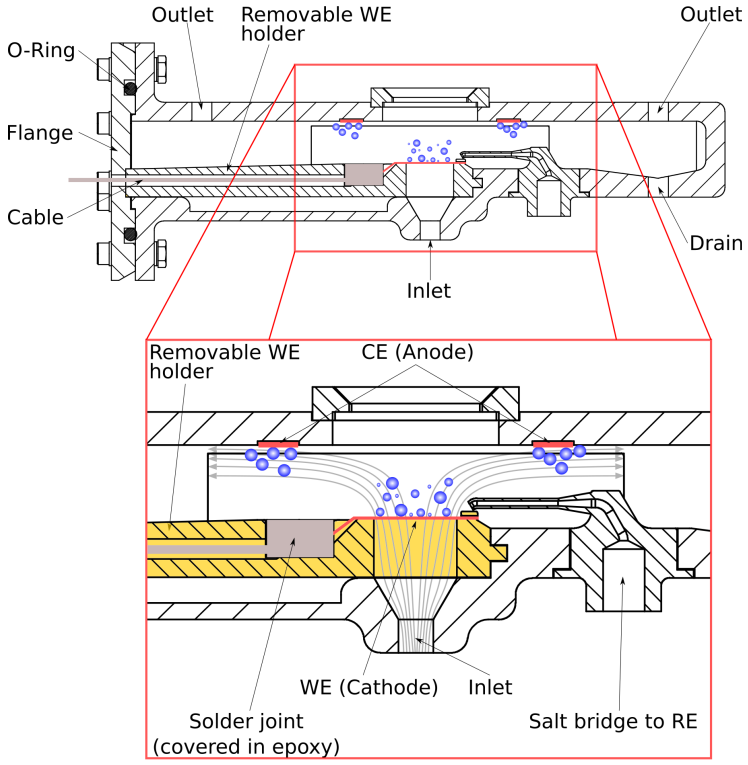

Figure 1: Schematic of the electrochemical cell consisting of three electrodes and a detailed view of the examined WE with indicated streamlines of the electrolyte flow. Note the two observation windows, detailed in Fig. 2, and the removable WE holder (highlighted in yellow).

Fig. 1 documents the schematic design of the 3D printed electrochemical cell. The bottom part of Fig. 1 is a magnified view of the electrodes comprising part of the cell. The electrochemical cell consists of a horizontally installed cathode (working electrode, WE) and two anodes (counter electrodes, CEs), as well as of a reversible hydrogen electrode (RHE, HydroFlex ®, Gaskatel, Germany) serving as a reference electrode (RE) connected to the cell via a salt bridge. The cathode is a section of expanded metal (EM) nickel of approx. $1 \times 10\,\mathrm{mm}^2$ (see Section 2.2) and the anode consists in two pieces of Pt foil (purity 99.95 %) together having an area of $\approx 100\,\mathrm{mm}^2$. The electrochemical cell features two observation windows and an easily exchangeable cathode holder [43]. It is worth emphasizing the possibility to simultaneously record side view and top view images of the hydrogen-forming cathode to capture the bubble evolution over time from two different perspectives (see Fig. 2). To allow the top view, the

anode electrode is produced as two pieces of foil at a distance from each other as shown in Fig. 1. The details of the electrochemical system are given in Section 2.3.

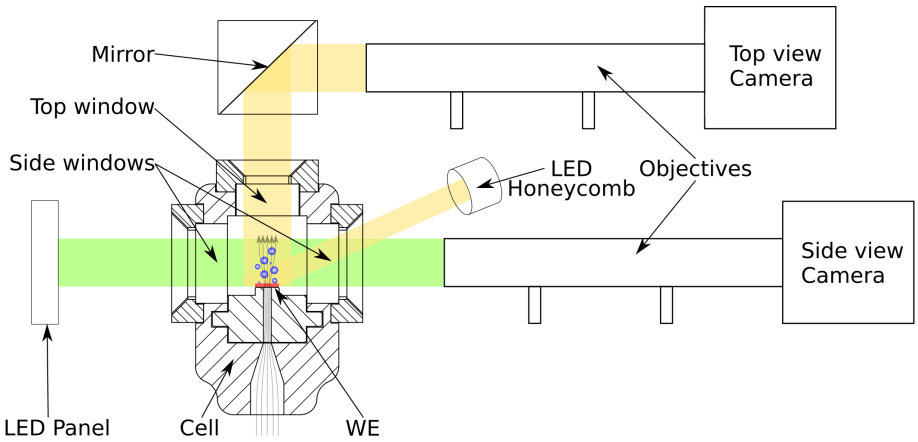

Figure 2: Schematics of the optical measurement system for both the top and side view images of the WE (colors are for illustration only)

The cell and the electrode holders were printed from DraftGrey (KOH resistant, Stratasys, USA) using an Objet30 Prime V5 (Stratasys, USA). The observation windows, made of PMMA (Poly(methyl methacrylate)), were glued into the cell using epoxy adhesive (Araldite 2013-1, Huntsman, USA). The configuration of the cell is T-shaped and therefore possesses one electrolyte flow inlet, located below the cathode, and two outlets located as shown in Fig. 2. The inlet and outlets are connected to separate reservoirs to avoid electrolyte remixing. To achieve a constant electrolyte flow without any pulsations, a microfluidic controller was used of the type OB1 MK3+ (Elveflow, France) with a maximum pressure of 2 bar. Within the scope of the present study, the possible mixing of H_2 and O_2 gases is tolerated, as the main focus is on the bubble dynamics at the cathode electrode of a different geometry. Therefore, no further precautions are taken to separate the products at the anode and cathode.

2.2. Fabricating the working electrode

Sections of expanded metal nickel (Benmetal, Germany) were cut with a laser into pieces of $1 \times 20\,\mathrm{mm}^2$. The cut electrodes were soldered to a copper wire ($d = 1\,\mathrm{mm}$) and glued to a 3D printed electrode holder using epoxy adhesive. The free surface area of the electrode was limited to approx. $1 \times 10\,\mathrm{mm}^2$ by covering the rest of the electrode area and the solder joint with epoxy. Afterwards, the electrodes were cleaned using deionized water and ethanol. To characterize the electrode surface, three nickel foils (GoodFellow, purity 99.99 %) were produced as benchmark electrodes in the same procedure, except that the surfaces of these foils were polished using 1 µm diamond polish and alumina polish (PK-4

Polishing Kit, BASi, USA) before the cleaning procedure. All the characteristic parameters of the expanded metal sections were determined by Benmetal using an OSIF MeshInspector ML system. In addition, the hydraulic diameter d_h was calculated using the following equation and assuming the pores to be diamond-shaped (see Fig. 3 and Table 1). For this purpose, the length, l_pore, and width, w_pore, of the mesh opening provided by Benmetal (see Supplemental Material) were used to calculate the area and perimeter of the pore (A_pore and P_pore). In the following, the electrodes are named according to the mesh width w_mesh, which is defined as the distance between the centres of two junctions in the direction of the short diagonal (see Fig. 3).

$$d_\mathrm{h} = \frac{4 \cdot A_\mathrm{pore}}{P_\mathrm{pore}} = \frac{w_\mathrm{pore} \cdot l_\mathrm{pore}}{\sqrt{w_\mathrm{pore}^2 + l_\mathrm{pore}^2}} \tag{1}$$

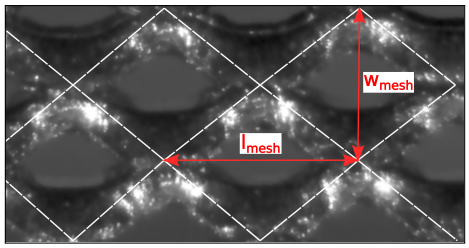

Figure 3: Image of one expanded nickel metal piece with diamond-shaped pores and the two essential parameters required to differentiate the electrodes: the mesh width w_mesh and the mesh length l_mesh

Table 1: Overview of the mesh width and length (w_mesh and l_mesh), the calculated hydraulic diameter d_h (see Eq. 1), the electrode porosity ε and electrode thickness t_el and the determined electrochemical characteristics, double-layer capacitance C_D and electrochemically active surface area $ECSA$ of the EM and the Ni benchmark electrodes Ni_bm

Name	$\boldsymbol{w}_\mathrm{mesh}$ in µm	$\boldsymbol{l}_\mathrm{mesh}$ in µm	$\boldsymbol{d}_\mathrm{h}$ in µm	$\boldsymbol{\varepsilon}$ in %	$\boldsymbol{t}_\mathrm{el}$ in µm	$\boldsymbol{C}_\mathrm{D}$ in µF	$\boldsymbol{ECSA}$ in cm^2
EM_475	475	600	136.13	22.6	75	12.1721	0.3453
EM_500	500	600	86.10	11.8	150	10.6417	0.3019
EM_518	518	602	100.86	15.5	200	17.6738	0.5014
Ni_bm	-	-	-	-	100	8.4916	0.2409

2.3. Electrochemical methods

The electrochemical experiments were carried out in 1 M KOH (Titripur, Merck, Germany) at 293 K in the three-electrode cell described above (see Section 2.1). The RE was placed in a separate syringe and connected to the cell through a salt bridge consisting of a 3D printed capillary and a tube

($d_{\mathrm{in}} = 0.5\,\mathrm{mm}$). All WE potentials were measured with respect to the RE using an electrochemical workstation (CHI660E, CH Instruments, USA).

To estimate the onset potential E_{O} of the hydrogen evolution reaction (HER) for all WEs, Linear Sweep Voltammetry (LSV) was performed over a potential range from 0 V to $-0.8\,\mathrm{V}$ at a scan rate of $\nu = 50\,\mathrm{mV\,s^{-1}}$. The onset potential E_{O} is defined as the intersection of the fitted tangent with the zero axis. Cyclic Voltammetry (CV) was used to calculate the double-layer capacitance C_{D} based on the following equation

$$C_{\mathrm{D}} = \frac{I_{\mathrm{a}} + |I_{\mathrm{c}}|}{2 \cdot \nu}, \tag{2}$$

where I_{a} is the absolute anodic current and I_{c} the cathodic current. The electrochemically active surface area $ECSA$ was determined by multiplying the calculated capacitance C_{D} with the ratio between $ECSA_{\mathrm{bm}}$ and $C_{\mathrm{D,\,bm}}$ of the smooth benchmark surface [44]. This is defined by the averaged surface of the three benchmark electrodes made out of plain nickel foil (see Section 2.2).

$$ECSA = C_{\mathrm{D}} \cdot \frac{ECSA_{\mathrm{bm}}}{C_{\mathrm{D,\,bm}}} \tag{3}$$

The measured electrochemically active surface area $ECSA$ was used to calculate the current I to be applied for achieving a specific current density j ($I = j \cdot ECSA$). For the imaging of the bubble nucleation, growth and detachment, galvanostatic measurements were performed at a sample rate of 50 Hz with various current densities ($j = -10, -20, -50, -100$ or $-200\,\mathrm{mA\,cm^{-2}}$).

Experimental parameters

For each WE, all measurements, including the electrochemical characterization, were performed under normal conditions (approx. $T = 293\,\mathrm{K}, p = 1\,\mathrm{bar}$) within the same day to avoid any contamination. Table 2 gives an overview of all experimental parameters. For each parameter set, three measurements were performed in order to obtain statistical confidence. Thus, a total of 3×5000 images were used for the side view evaluation and 3×1000 for the top view evaluation. Fewer images were used for the top view because the rising bubbles tended to cover the observation window over time. The galvanostatic measurements were performed over a period of 20 s.

2.4. Imaging and image processing

Two high-speed cameras (IDT OS-7 S3, USA), each equipped with a precision micro-imaging lens with a magnification of 2 (Optem® FUSION, USA), were used at a sample rate of 500 fps and a bit depth of 12 bit. The spatial resolution of the side view and top view cameras was 593 px/mm and 505 px/mm, respectively. Both calibrations were performed using a dual-axis linear scale micrometer with a scale division of 25 µm (Edmund Optics, USA). Greater details on the camera settings in the form of metadata can be found in the Supplemental Material (.hdf5 files). To complete the shadowgraphy system, one LED

Table 2: Overview of the varied parameters, the applied current density j, electrolyte flow rate $\dot{V}$, electrochemically active surface area $ECSA$ and electrode porosity ε, as well as the constant experimental parameters, the electrolyte concentration c_{KOH} used and the free surface of the Pt-CE A_{CE}

	Parameter	Description
Varying	j	-10, -20, -50, -100, $-200\,\mathrm{mA\,cm^{-2}}$
	$\dot{V}$	0 and $5\,\mathrm{ml\,min^{-1}}$
	$ECSA$	30.19, 34.53, $50.14\,\mathrm{mm^2}$ (see Table 1)
	ε	11.8, 15.5, 22.6 % (see Table 1)
Const	c_{KOH}	1 M KOH
	A_{CE}	$80\,\mathrm{mm^2}$

panel (CCS TH2, Japan) and two honeycomb LEDs (IDT, USA) were incorporated, providing back and top illumination, respectively. The side view images were used to calculate the size of the bubbles at the detachment, whereas the top view images made it possible to estimate the electrode coverage over time. The image analysis procedures were performed in Python 3.8.

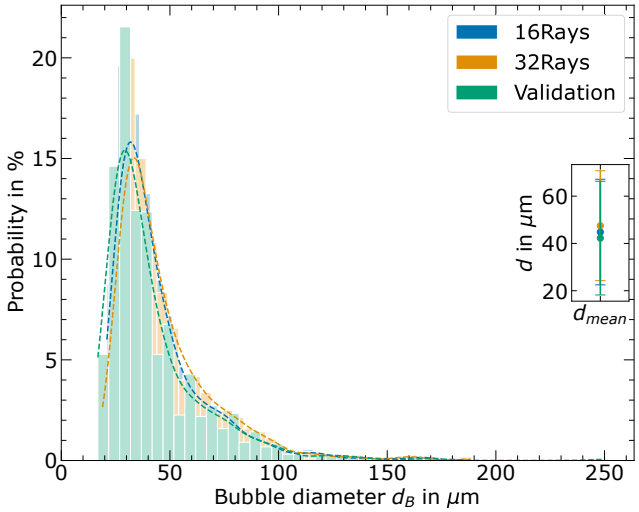

Figure 4: Bubble size distribution with dashed fit for better comparison and mean bubble diameter (plotted in inset axis) for two different stardist models (16 rays (blue) and 32 rays (orange)) in comparison to the validation data set (green) with semi-automatically annotated bubbles showing a good agreement of both models

The detection of single bubbles using conventional, well-established algorithms such as the Hough transform becomes especially challenging at high current densities, where a high fraction of gas bubbles overlap. Therefore, an approach based on machine learning was applied using stardist [45, 46]. The

stardist method is based on the prediction of the object probability $d_{i,j}$ and the Euclidean distance $r^{k}_{i,j}$ along k radial rays. Each bubble is described by multiple rays as a star-convex polygon. These were fitted as an ellipse to calculate the bubble diameters d_B [47]. Since the key criterion in the present analysis is the precise detection of the bubble size distribution, the bubble size d_B is used as a criterion for evaluating the model. Two different stardist models, 16 or 32 rays, respectively, were compared to an evaluation set of randomly chosen set of 100 images (see Supplemental Material). A comparison of the results (see Fig. 4) led to the choice of the model using 16 rays, as the deviation is minimal. Therefore, only the results calculated with the 16-ray model will be discussed in the following. Since the evolving H_2 bubbles can be described as spheres, the number of 16 points from the rays at the bubble boundary is also enough for the ellipse fitting algorithm.

Another advantage of stardist is that less image preprocessing is needed. Only the region of interest (ROI) needs to be cropped out of the image and the bubbles are detected using the trained model. As stacks of bubbles form at the electrode (see Fig. 5a), a rectangular region with a width of 30 px at the top of the images was chosen as the ROI to ensure that only detached bubbles are processed. The postprocessing is split into deleting blurred bubbles and linking all those remaining (see Fig. 5b-c). The phenomenon underlying blurred bubbles is the depth of field (DOF) of the optical system. By moving the calibration plate through the plane of focus, the DOF could be estimated as $\approx 66\,\mu m$ (see Supplemental Material). The variance in the Laplacian of the single bubble was chosen as the criterion to define a bubble inside the measurement plane. Since this value is dependent on the bubble size d_B or the size of the image section, respectively, a threshold is applied first for deleting misdetected objects ($Var(\Delta) < 50$). The variance is then multiplied by the bubble diameter d_B to guarantee that all bubble sizes are treated equally. Next, the blur criterion is applied, which is sketched in Fig. 6 as a dashed red line and is defined as the 30% quantile of the distribution of the calculated metric ($Var(\Delta) \cdot d_B^2$) over all bubbles. The detected, processed bubbles were linked using trackpy [48] to cal-

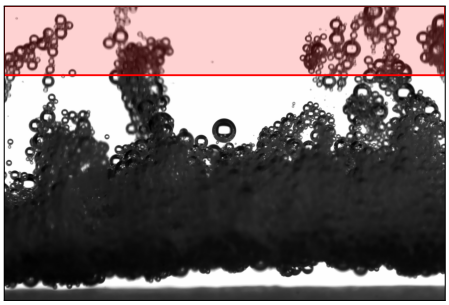

(a) Raw image of side view analysis

(b) Cropped ROI

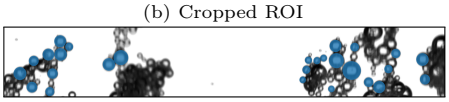

(c) Result with annotated bubbles for all bubbles detected using stardist

Figure 5: Processing of side view images consisting of cropping the ROI, detecting the bubbles using stardist and post-processing (deleting blurred bubbles and misdetected objects)

culate the mean diameter d_{m} of each bubble and avoid one bubble being counted multiple times when measuring the size distribution of the detached bubbles. Additionally, the standard deviation of d_{m} was calculated during the crossing of the ROI and only the bubbles with $Var(d_{\mathrm{m}}) < 1$ were taken into account for the bubble size distributions. This procedure ensures that misdetected bubbles are excluded from further consideration as far as possible.

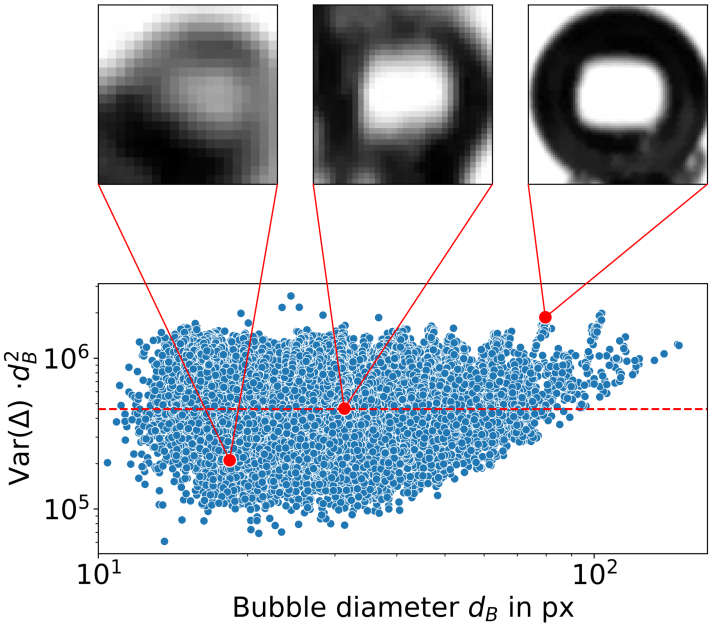

Figure 6: Blur criterion (dashed red line) to distinguish between blurred and sharp bubbles with example images of a blurred and a sharp bubble, as well as a bubble in the transition area

The overall electrode coverage was calculated from the top view images using the structural similarity (SSIM) function included in scikit-image [49, 50]. The SSIM index is a measure of the structural similarity of two images, comparing their luminance, contrast and structure [49]. One advantage of the SSIM index is that the result is not influenced by the non-homogeneous illumination of the top view images [50]. As the laser-cut edges of the electrodes are not representative of the electrode performance, only the central part of the electrode was processed. First, the image of the clean electrode is divided by an average background image. All subsequent frames are then compared to this image using the SSIM function. A sliding window with a size of 9 pixels, thus $\approx 18 \times 18\,\mu\mathrm{m}^2$, is used and the local SSIM index is calculated by comparing it with the same section of the average background image. The size of the sliding window was chosen to guarantee a robust result and to simultaneously resolve the structure of the electrodes. By applying a simple threshold on the calculated SSIM image, the non-zero pixels can be counted; they correspond to those parts

of the electrode covered by bubbles. The total coverage of the electrode A_{cov} is calculated using the given values for the electrode porosity ε (see. Table 1) and is defined as

$$A_{\mathrm{cov}} = \frac{N}{A_{\mathrm{im}} \cdot (1 - \varepsilon)}, \tag{4}$$

where N is the total number of non-zero pixels in the threshold image (see Fig. 7d) and A_{im} is the size of the cropped image. The processing of top view images is sketched in Fig. 7.

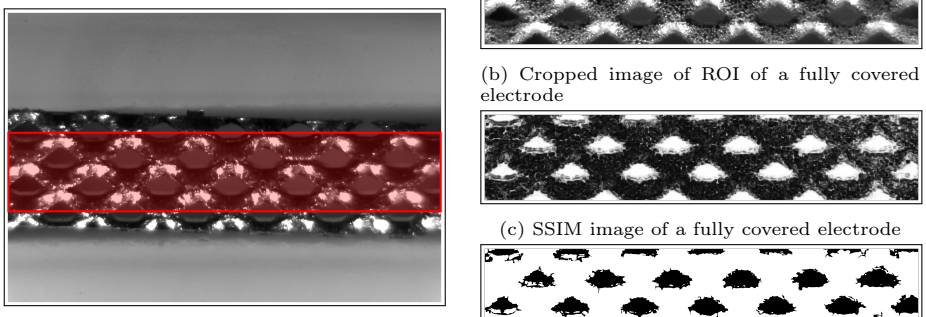

(a) Raw image of the clean electrode

(b) Cropped image of ROI of a fully covered electrode

(c) SSIM image of a fully covered electrode

(d) Image with applied threshold to calculate the electrode coverage

Figure 7: Image processing of top view images consisting of cropping the ROI, calculating the SSIM image of each image by comparing it with the image of the clean electrode and counting the non-zero pixels

All processed data including example videos are available at 10.14278/rodare.1845.

3. Results and discussion

3.1. Electrochemical characterization and performance of electrodes

The double-layer capacitance C_{D} was measured by applying electric potentials at which no significant Faradaic reaction occurs, such that the small current I measured only stems from charging/discharging of the electrode according to the double-layer capacitance C_{D} (see Fig. 8b) [51]. By running a CV in a wide potential window from 0.25 V to 0.85 V, the potential range of 0.75 V to 0.85 V was obtained. As can be seen in Fig. 8a, nearly rectangular cyclic voltammograms were measured, suggesting that the chosen potential range is suitable, and the measured current corresponds to charging and discharging of the electrode. Thus, the $ECSA$ calculated in accordance with Eq. 3 corresponds to the electrochemically active surface of the electrode. It is important to emphasize that differences in the measured $ECSA$ can be caused by the material properties (e.g. impurities or enhanced roughness) or different geometrical sizes of

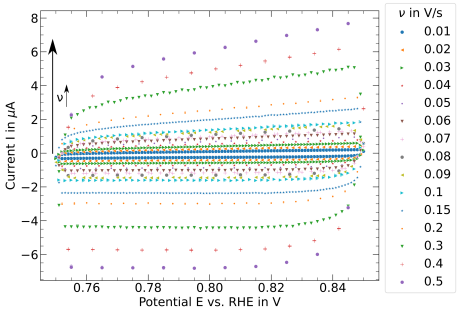

(a) CVs at 15 different scan rates for the electrode *EM_475*

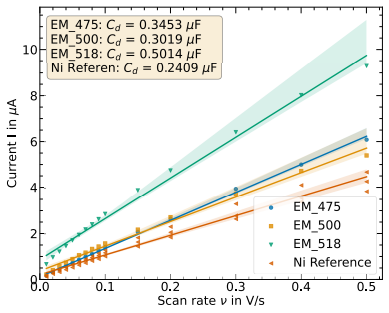

(b) Linear fits of current $I = I_a + |I_c|$ over scan rate ν to calculate double-layer capacitance C_D of each electrode

Figure 8: Capacitance measurements to calculate $ECSA$ for all three expanded metal nickel sections using CV

the uncovered electrode surface. However, all expanded metals show a bigger $ECSA$ compared to the plain nickel foils.

The onset potential for HER, E_O, was determined using LSV (see section 2.3). Fig. 9 shows that E_O is similar for all the expanded metals. Since all the expanded metals were made of nickel with the same purity and were produced with similar manufacturing parameters, this is reasonable. In summary, the main differences between the expanded metals studied lie in the hydraulic diameter d_h and the $ECSA$. This also takes into account the different thicknesses t_{el} of the electrodes (see Table 1).

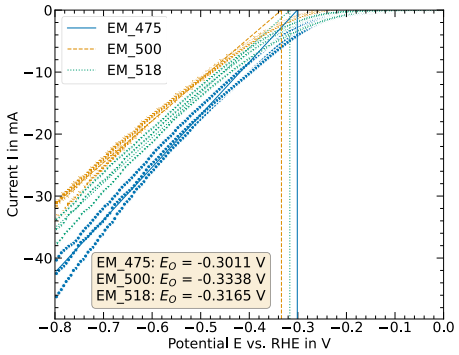

Figure 9: Measured current I during LSV from 0 V to −0.8 V to determine the onset potential E_O as the intersection of the fitted tangent with the line of $I = 0$ mA for three different expanded nickel metals

One aspect that is crucial for the overall efficiency of the electrolysis is the electrochemical performance of the electrodes, which can be described using the

voltage efficiency η_{E}

$$\eta_{\mathrm{E}} = \frac{|\Delta E^0|}{\Delta E(j)}, \tag{5}$$

where $|\Delta E^0| = 1.23\,\mathrm{V}$ is the reversible cell potential for the water splitting reaction under standard conditions and $\Delta E(j)$ is the measured cell potential at a specific current density j [19]. $\Delta E(j)$ is defined as the sum of $|\Delta E^0|$ and the absolute value of the overpotential losses:

$$\Delta E(j) = |\Delta E^0| + |\eta_{\mathrm{HER}}| + \eta_{\mathrm{OER}} + \eta_{\Omega} + \eta_{\mathrm{conc}} \tag{6}$$

According to Pang et al. [19], the concentration overpotential η_{conc} is negligible in strong bases. Since all tests were carried out under the same conditions with the same CE, not only $|\Delta E^0|$ but also the overpotential of the oxygen evolution reaction (OER) η_{OER} can be assumed to be constant. Thus, a larger measured $\Delta E(j)$ corresponds to greater ohmic overpotential losses η_{Ω} and HER related losses η_{HER}.

In Fig. 10, the average potential $\bar{E}$ and standard deviation σ of the quasi-steady state region in the time span of $t = 8 \ldots 10\,\mathrm{s}$ are plotted over all the current densities $|j|$ studied. In general, greater overpotential losses of the electrode *EM_518* are observed. Additionally, for each electrode, two curves are plotted in Fig. 10 for the cases with and without flow-through. It can be stated that the flow-through has a negligible effect on the potential E for all electrodes and all current densities j. Although this is not what flow-through is intended to achieve in membraneless electrolyzers, the phenomenon might be strongly influenced by the specific design of our test cell where the focus is solely on the cathode side, whereas the flow-by situation at the anodes is far from being optimal. For all the parameters studied, the electrode *EM_518* shows the highest potential $E(j)$. Since the applied current I was defined by the calculated area $ECSA$, it can be concluded that the overpotential η_{HER} of the electrode *EM_518* is greater compared to the other electrodes, assuming constant η_{OER} at the Pt-CE.

3.2. Bubble size distributions

The analysis of the size of detached bubbles d_{32} is crucial when designing and selecting operating conditions for membraneless electrolyzers such that the overall efficiency and the product purity are maximized [17]. When considering the gas crossover within the electrode gap, the detached bubble diameter d_{B} has to be minimized in order to reduce the electrode gap. Since a large electrode gap acts as a bottleneck in membraneless electrolyzers compared to other well-established technologies, it must be reduced, though only as long as product purity remains guaranteed.

In Fig. 11, the dependence of the WE on the size distribution of detached bubbles is shown when two different current densities are applied, $|j| = 20\,\mathrm{mA\,cm^{-2}}$ and $|j| = 100\,\mathrm{mA\,cm^{-2}}$. To provide additional information, the

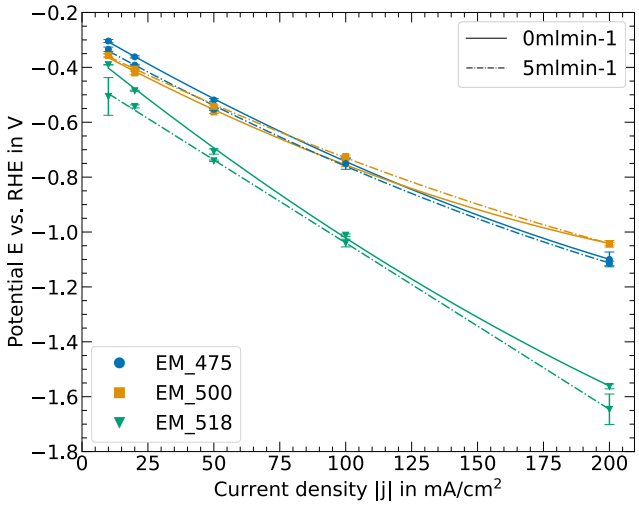

Figure 10: Electrochemical performance of the electrodes *EM_475*, *EM_500* and *EM_518* over a current density range from $|j| = 20$ to $200\,\mathrm{mA\,cm^{-2}}$ and at two different flow rates using the averaged potential $\bar{E}$ vs. RHE of the quasi-steady state region ($t = 8 \ldots 10\,\mathrm{s}$) under galvanostatic conditions

average diameter d_m and Sauter diameter d_{32} are calculated and plotted for each distribution. Due to the limited spatial resolution, all bubble size distributions are cut off at a bubble diameter of $d_\mathrm{cutoff} \approx 20\,\mu\mathrm{m}$ and must be taken into account for all further analysis. Especially at low current densities of $|j| \leq 20\,\mathrm{mA\,cm^{-2}}$ (see Fig. 11a), slight differences between the electrodes can be measured. E.g., *EM_518* shows a smaller mean diameter d_m and Sauter diameter d_{32} as well as a narrower bubble size distribution. For a better visualization of the results for all parameter variations, in the following only the Sauter diameter d_{32} will be taken into account.

For the electrode *EM_518*, a correlation can be identified between the size distribution of detached bubbles and the current density $|j|$. Increasing current densities $|j|$ lead to increasing Sauter diameters d_{32} (see Fig. 12) and a wider distribution, as shown in Fig. 11. Increasing bubble sizes were also reported by Luo et al. [52] in their study of inexpensive and efficient electrocatalysts for hydrogen evolution. This phenomenon can be seen for all studied electrodes especially clearly if an electrolyte flow is applied (see Fig. 12), even at the low flow rates $\dot{V}$ applied during the study. The bubble size is drastically reduced (by as much as $\approx 40\%$ at a current density of $|j| = 10\,\mathrm{mA\,cm^{-2}}$), when the electrolyte flow is applied through the electrodes compared to the no-flow condition. By increasing the electrolyte flow rate $\dot{V}$, the shear rate at the electrode-bubble interface increases proportionally. Thus, the bubbles detach faster and at a smaller Sauter diameter d_{32}. A similar effect of premature departure due to the applied electrolyte flow was observed by Zhang and Zeng [53]. Thus, the shear rate is a fundamental parameter to adjust the bubble size and also the product

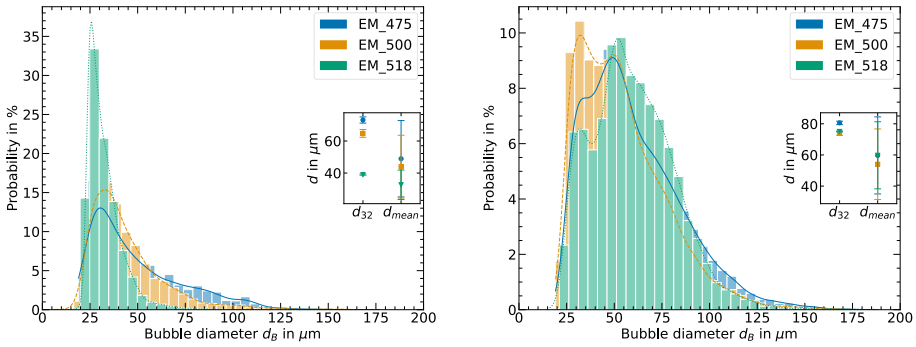

(a) Current density $|j| = 20\,\mathrm{mA\,cm^{-2}}$ (b) Current density $|j| = 100\,\mathrm{mA\,cm^{-2}}$

Figure 11: Size distribution with fitted curves of the detached H_2 bubbles at two different current densities $|j|$ and a flow rate of $5\,\mathrm{ml\,min^{-1}}$ for 3 different expanded nickel metals and additional plots of the mean bubble diameter d_m and Sauter diameter d_{32}

purity in applications such as membraneless electrolyzers. However, the effect of the flow rate falls as the current density $|j|$ increases. This may be due to the fact that the bubble growth rate and the number of nucleation centers increase with the current density $|j|$. Therefore, at high current densities $|j|$, the low flow rate $\dot{V}$ applied and thus also the low shear rate no longer influence the bubble growth and detachment so strongly. Here, further experiments including also higher flow rates $\dot{V}$ are necessary to derive reliable trends at higher current densities j.

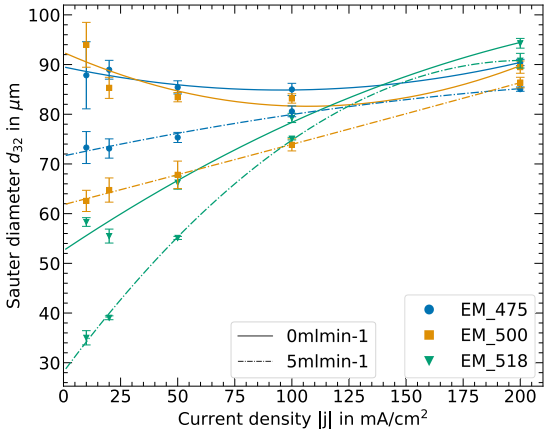

Figure 12: Sauter diameter d_{32} of the detached H_2 bubbles as a function of the applied current density $|j|$ and the flow rate $\dot{V}$

However, the electrodes *EM_ 518* and *EM_ 500* show nearly constant Sauter diameters d_{32} for the no-flow condition compared to the electrode *EM_ 518*. In general, the Sauter diameter d_{32} is much less affected by an increase of the

current density j without flow. This might indicate that the bubble size is determined by the electrode geometry and electrochemical properties. Here, the electrodes *EM_ 518* and *EM_ 500* show similar electrochemical performance and the electrode *EM_ 518* shows clear differences (see Fig. 10).

It is important to mention that even though the approach based on machine learning leads to better results at higher current densities, many bubbles cannot be detected. This is not due to the algorithm, but to the non-transparent bubble plume detaching at high current densities $|j|$. Within the plume, only big bubbles at the edge of the bubble plumes can usually be segmented. Hence, the bubble size distributions at high current densities $|j|$ are likely to lack small bubbles. However, the correlation of increasing bubble sizes d_{32} with increasing current density $|j|$ remains valid. Additionally, as the current density $|j|$ increases, not only the size of detached bubbles d_{32} but also the bubble layer thickness increases. All of this together leads finally to an increase in the overpotential η_{HER} [54].

3.3. Electrode coverage

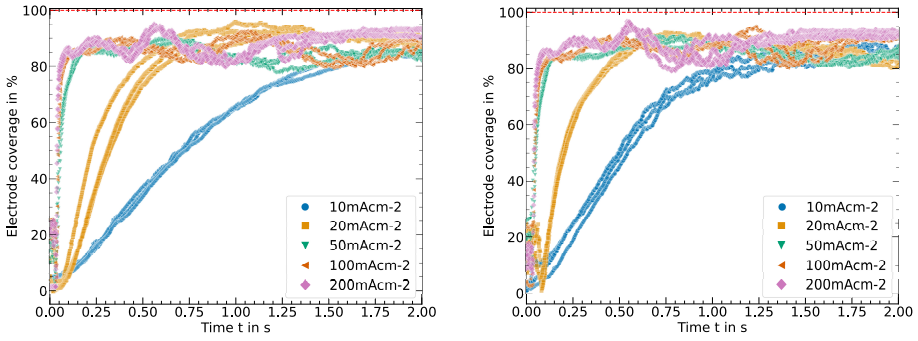

(a) Flow rate $\dot{V} = 0\,\mathrm{ml\,min^{-1}}$ (b) Flow rate $\dot{V} = 5\,\mathrm{ml\,min^{-1}}$

Figure 13: Dependance of the applied current density $|j|$ and the flow rate $\dot{V}$ on the coverage of the WE A_{cov} over time shown by way of example for the WE *EM_ 500*

Fig. 13 shows the development of the surface coverage A_{cov} over time at different current densities $|j|$ and flow rates $\dot{V}$ for the WE *EM_ 500*. For current densities larger than $|j| \geq 50\,\mathrm{mA\,cm^{-2}}$ the electrode is nearly fully covered in less than 0.1 s, whereas it takes significantly longer at low current density $|j|$ (see Fig. 13). This can be observed for both flow rates $\dot{V}$. By plotting the time t at which the maximum coverage of each WE is reached over all the current densities $|j|$ studied (see Fig. 14), the fast covering of the electrode at current densities larger than $|j| \geq 50\,\mathrm{mA\,cm^{-2}}$ can be found for all the electrodes studied. Thus, with an increasing current density $|j|$ the electrode is covered in a shorter timescale. By contrast, the flow rate $\dot{V}$ shows a negligible effect on the coverage A_{cov}. However, it is interesting to note that the tendency is for the electrode to be covered more rapidly in the presence of an electrolyte flow.

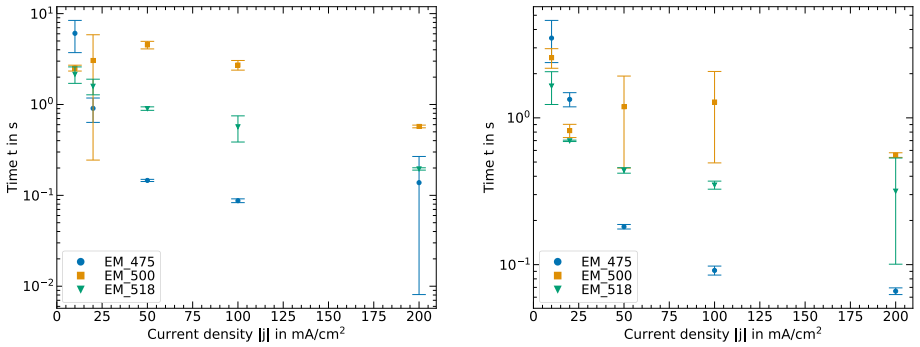

(a) Flow rate $\dot{V} = 0\,\mathrm{ml\,min^{-1}}$ (b) Flow rate $\dot{V} = 5\,\mathrm{ml\,min^{-1}}$

Figure 14: Time t at which the WE surface reached maximal coverage for the different WEs and at electrolyte flowrates of 0 or $5\,\mathrm{ml\,min^{-1}}$

The images of the top view have a low spatial resolution, an issue that could not be improved due to difficulties with illumination. Thus, coverages below $A_{\mathrm{cov}} \approx 20\,\%$ could not be resolved. Nevertheless, the results show that the current density $|j|$ significantly influences the surface coverage of all the WEs studied. This agrees with Faraday's law, which describes the proportionality between the electric charge and evolved gas, and with the studies by Vogt [42] for low current densities $|j|$. Since the camera and the electrochemical signal were not synchronized, the deviation of the calculated time t in Fig. 14 reaches values of ≈ 50 %. In future experiments, this will be avoided by using a trigger signal. Furthermore, since the bubbles rise against the observation window, especially when an electrolyte flow $\dot{V}$ is applied, the tendency for the coverage time A_{cov} to decrease is affected by an additional source of uncertainty: bubbles that are already detached and rising.

4. Conclusion and Outlook

This study has introduced a new cell type to perform parametrical studies on various electrodes. Importantly, the cell features a combined analysis of two different perspectives, the top view and side view, that can be used to validate improvements in the bubble dynamics of newly developed electrodes, such as laser-structured or coated electrodes. Moreover, an approach based on machine learning was used to study the size distribution of detached bubbles as a characteristic value for the WE. Additionally, the bubble coverage of the electrode A_{cov} was taken into account. Thus, a complete characterization of various electrodes is possible and can help in individual cases to decide which electrode to use. This also makes the cell interesting for the development of new electrodes, since the WE can be characterized holistically.

The electrodes studied showed similar behaviors for all experimental parameters. Only the expanded nickel metal *EM_518* showed higher overpotential

η_{HER}. The greatest impact of the applied flow rate $\dot{V}$ was observed at low current densities ($|j| \leq 50\,\mathrm{mA\,cm^{-2}}$), where the size of detached bubbles d_{32} was reduced by as much as $\approx 40\%$. In further experiments, the flow rate $\dot{V}$ must be increased to gain a better understanding of the shear rate's influence on the bubble growth and detachment, respectively. Additionally, the current density j is affecting the detached bubble size as well as the electrode coverage A_{cov}. In general, it can be stated that increasing current densities lead to a faster covering of the electrodes. By increasing the applied current density j, the Sauter diameter d_{32} also tends to increase. However, due to the evolving bubble plumes at high current densities j the results lack in small bubbles entrapped inside these plumes.

After this proof-of-concept, the cell will be used to run parametric studies on structured electrodes and on different manufacturing methods. By further optimizing the stardist models and increasing the spatial resolution, it might be possible to investigate bubble dynamics at even higher current densities.

Conflicts of interest

There are no conflicts to declare.

Acknowledgments

The Helmholtz Association of German Research Centres (HGF), and German Federal Ministery of Education and Research (BMBF) is gratefully acknowledged for supporting the development of solar powered H_2 generation technologies within the frame of the Innovation Pool Project "Clean and Compressed Solar H_2". Furthermore, financial support by the BMBF under contract No. 03SF0672 is gratefully acknowledged. The responsibility for the paper's content is with the authors.

Nomenclature

Latin Symbols

A	Electrode area in $\mathrm{m^2}$
A_{CE}	Counter electrode area in $\mathrm{m^2}$
A_{cov}	Covered electrode area in $\mathrm{m^2}$
A_{im}	Image size in $\mathrm{px^2}$
A_{pore}	Area of the pore in $\mathrm{m^2}$
C_{D}	Electrode double-layer capacitance in F
c_{KOH}	Electrolyte concentration in M
d_{B}	Bubble diameter in m
d_{cutoff}	Cutoff diameter of spatial resolution in m
d_{h}	Hydraulic diameter in m
$d_{\mathrm{i,j}}$	Object probability (stardist)

d_{in}	Inner diameter in m
d_{m}	Mean diameter in m
d_{32}	Sauter diameter in m
$ECSA$	Electrochemically active surface area in m^2
ΔE^0	Reversible cell potential for the water splitting reaction under standard conditions in V
E	Potential in V
E_{O}	Onset potential in V
I	Electrical current in A
I_{a}	Anodic current in A
I_{c}	Cathodic current in A
j	Current density in $\mathrm{A\,cm^{-2}}$
k	Number of radial rays (stardist)
l_{mesh}	Mesh length in m
l_{pore}	Pore length in m
N	Number of pixels
p	Pressure in Pa
P_{pore}	Perimeter of the pore in m
$r_{\mathrm{i,j}}$	Euclidean distance in m (stardist)
T	Temperature in K
t	Time in s
t_{el}	Electrode thickness in m
$\dot{V}$	Flow rate in $\mathrm{m^3\,s^{-1}}$
w_{mesh}	Mesh width in m
w_{pore}	Pore width in m

Greek Symbols

η_{Ω}	Ohmic overpotential in V
η_{conc}	Concentration overpotential in V
η_{E}	Voltage efficiency in %
η_{HER}	Overpotential of the hydrogen evolution reaction in V
η_{OER}	Overpotential of the oxygen evolution reaction in V
ν	Scan rate in $\mathrm{V\,s^{-1}}$
σ	Standard deviation
ε	Porosity in %

References

[1] S. van Renssen. The hydrogen solution? *Nature Climate Change*, 10(9): 799–801, 2020. doi:10.1038/s41558-020-0891-0.

[2] M. van der Spek, C. Banet, C. Bauer, P. Gabrielli, W. Goldthorpe, M. Mazzotti, S. T. Munkejord, N. A. Røkke, N. Shah, N. Sunny, D. Sutter, J. M. Trusler, and M. Gazzani. Perspective on the hydrogen economy as a pathway to reach net-zero co2 emissions in europe. *Energy Environmental Science*, 15:1034–1077, 2022. doi:10.1039/D1EE02118D.

[3] I. Staffell, D. Scamman, A. V. Abad, P. Balcombe, P. E. Dodds, P. Ekins, N. Shah, and K. R. Ward. The role of hydrogen and fuel cells in the global energy system. *Energy & Environmental Science*, 12(2):463–491, 2019. doi:10.1039/c8ee01157e.

[4] T. Smolinka and J. Garche. *Electrochemical Power Sources: Fundamentals, Systems, and Applications: Hydrogen Production by Water Electrolysis*. Elsevier, 2021. ISBN 9780128194256.

[5] D. Milani, A. Kiani, and R. McNaughton. Renewable-powered hydrogen economy from australia's perspective. *International Journal of Hydrogen Energy*, 45(46):24125–24145, 2020. doi:10.1016/j.ijhydene.2020.06.041.

[6] N. Sazali. Emerging technologies by hydrogen: A review. *International Journal of Hydrogen Energy*, 45(38):18753–18771, 2020. doi:10.1016/j.ijhydene.2020.05.021.

[7] European Comission. A hydrogen strategy for a climate-neutral europe. https://ec.europa.eu/energy/sites/ener/files/hydrogen_strategy.pdf, 2020. Accessed: 2022-06-14.

[8] A. Angulo, P. van der Linde, H. Gardeniers, M. Modestino, and D. F. Rivas. Influence of bubbles on the energy conversion efficiency of electrochemical reactors. *Joule*, 4(3):555–579, 2020. doi:10.1016/j.joule.2020.01.005.

[9] X. Zhao, H. Ren, and L. Luo. Gas bubbles in electrochemical gas evolution reactions. *Langmuir*, 35(16):5392–5408, 2019. doi:10.1021/acs.langmuir.9b00119.

[10] J. A. Leistra and P. J. Sides. Voltage components at gas evolving electrodes. *Journal of the Electrochemical Society*, 134(10):2442, 1987. doi:10.1149/1.2100218.

[11] J. R. Lake, Á. M. Soto, and K. K. Varanasi. Impact of bubbles on electrochemically active surface area of microtextured gas-evolving electrodes. *Langmuir*, 2022. doi:10.1021/acs.langmuir.2c00035.

[12] D. V. Esposito. Membraneless Electrolyzers for Low-Cost Hydrogen Production in a Renewable Energy Future. *Joule*, 1:651–658, 2017. doi:10.1016/j.joule.2017.07.003.

[13] M. I. Gillespie, F. van der Merwe, and R. J. Kriek. Performance evaluation of a membraneless divergent electrode-flow-through (DEFT) alkaline electrolyser based on optimisation of electrolytic flow and elctrode gap. *Journal of Power Sources*, 293:228–235, 2015. doi:10.1016/j.jpowsour.2015.05.077.

[14] M. I. Gillespie and R. J. Kriek. Hydrogen production from a rectangular horizontal filter press Divergent Electrode-Flow-Through (DEFT) alkaline electrolysis stack. *Journal of Power Sources*, 372:252–259, 2017. doi:10.1016/j.jpowsour.2017.10.080.

[15] M. I. Gillespie and R. J. Kriek. Scalable hydrogen production from a mono-circular filter press Divergent Electrode-Flow-Through alkaline electrolysis stack. *Journal of Power Sources*, 397:204–213, 2018. doi:10.1016/j.jpowsour.2018.07.026.

[16] J. C. Bui, J. T. Davis, and D. V. Esposito. 3D-Printed electrodes for membraneless water electrolysis. *Sustainable Energy & Fuels*, 4:213–225, 2020. doi:10.1039/c9se00710e.

[17] J. T. Davis, D. E. Brown, X. Pang, and D. V. Esposito. High Speed Video Investigation of Bubble Dynamics and Current Density Distributions in Membraneless Electrolyzers. *Journal of the Electrochemical Society*, 166: F312–F321, 2019. doi:10.1149/2.0961904jes.

[18] G. D. O'Neil, C. D. Christian, D. E. Brown, and D. V. Esposito. Hydrogen Production with a Simple and Scalable Membraneless Electrolyzer. *Journal of The Electrochemical Society*, 163:F3012–F3019, 2016. doi:10.1149/2.0021611jes.

[19] X. Pang, J. T. Davis, A. D. Harvey Ill, and D. V. Esposito. Framework for evaluating the performance limits of membraneless electrolyzers. *Energy & Environmental Science*, 13:3663–3678, 2020. doi:10.1039/d0ee02268c.

[20] S. M. H. Hashemi, M. A. Modestino, and D. Psaltis. A membrane-less electrolyzer for hydrogen production across the pH scale. *Energy & Environmental Science*, 8:2003–2009, 2015. doi:10.1039/c5ee00083a.

[21] S. M. H. Hashemi, P. Karnakov, P. Hadikhani, E. Chinello, S. Litvinov, C. Moser, P. Koumoutsakos, and D. Psaltis. A versatile and membraneless electrochemical reactor for the electrolysis of water and brine. *Energy & Environmental Science*, 12(5):1592–1604, 2019. doi:10.1039/c9ee00219g.

[22] H. Dotan, A. Landman, S. W. Sheehan, K. D. Malviya, G. E. Shter, D. A. Grave, Z. Arzi, N. Yehudai, M. Halabi, N. Gal, N. Hadari, C. Cohen, A. Rothschild, and G. S. Grader. Decoupled hydrogen and oxygen evolution by a two-step electrochemical–chemical cycle for efficient overall water splitting. *Nature Energy*, 4(9):786–795, 2019. doi:10.1038/s41560-019-0462-7.

[23] X. Yan, J. Biemolt, K. Zhao, Y. Zhao, X. Cao, Y. Yang, X. Wu, G. Rothenberg, and N. Yan. A membrane-free flow electrolyzer operating at high current density using earth-abundant catalysts for water splitting. *Nature Communications*, 12(1), 2021. doi:10.1038/s41467-021-24284-5.

[24] V. Solovey, M. Zipunnikov, A. Shevchenko, I. Vorobjova, and A. Kotenko. Energy Effective Membrane-less Technology for High Pressure Hydrogen Electro-chemical Generation. *French-Ukrainian Journal of Chemistry*, 6: 151–156, 2018. doi:10.17721/fujcV6I1P151-156.

[25] V. Solovey, N. T. Khiem, M. Mykolaevich Zipunnikov, and A. Shevchenko. Improvement of the Membrane - less Electrolysis Technology for Hydrogen and Oxygen Generation. *French-Ukrainian Journal of Chemistry*, 6:73–79, 2018. doi:10.17721/fujcV6I2P73-79.

[26] V. Solovey, A. Shevchenko, M. Zipunnikov, A. L. Kotenko, N. T. Khiem, B. D. Tri, and T. T. Hai. Development of high pressure membraneless alkaline electrolyzer. *International Journal of Hydrogen Energy*, 2021. doi:10.1016/j.ijhydene.2021.01.209.

[27] H. Rajaei, A. Rajora, and J. W. Haverkort. Design of membraneless gas-evolving flow-through porous electrodes. *Journal of Power Sources*, 491: 229364, 2021. doi:10.1016/j.jpowsour.2020.229364.

[28] X., D. Baczyzmalski, C. Cierpka, G. Mutschke, and K. Eckert. Marangoni convection at electrogenerated hydrogen bubbles. *Physical Chemistry Chemical Physics*, 20(17):11542–11548, 2018. doi:10.1039/c8cp01050a.

[29] A. Bashkatov, S. S. Hossain, X. Yang, G. Mutschke, and K. Eckert. Oscillating Hydrogen Bubbles at Pt Microelectrodes. *Physical Review Letters*, 132, 2019. doi:10.1103/PhysRevLett.123.214503.

[30] S. S. Hossain, G. Mutschke, A. Bashkatov, and K. Eckert. The thermocapillary effect on gas bubbles growing on electrodes of different sizes. *Electrochimica Acta*, 353:136461, 2020. doi:10.1016/j.electacta.2020.136461.

[31] A. M. Meulenbroek, A. W. Vreman, and N. G. Deen. Competing marangoni effects form a stagnant cap on the interface of a hydrogen bubble attached to a microelectrode. *Electrochimica Acta*, page 138298, 2021. doi:10.1016/j.electacta.2021.138298.

[32] S. S. Hossain, A. Bashkatov, X. Yang, G. Mutschke, and K. Eckert. Force balance of hydrogen bubbles growing and oscillating on a microelectrode. *Physical Review E*, 106:035105, 2022. doi:10.1103/PhysRevE.106.035105.

[33] A. Bashkatov, S. S. Hossain, G. Mutschke, X. Yang, H. Rox, I. M. Weidinger, and K. Eckert. On the growth regimes of hydrogen bubbles at microelectrodes. *Accepted in Physical Chemistry Chemical Physics*, 2022.

[34] Y. Zhang, M. D. Merrill, and B. E. Logan. The use and optimization of stainless steel mesh cathodes in microbial electrolysis cells. *International Journal of Hydrogen Energy*, 35(21):12020–12028, 2010. doi:10.1016/j.ijhydene.2010.08.064.

[35] L. Li, W. Jiang, G. Zhang, D. Feng, C. Zhang, W. Yao, and Z. Wang. Efficient mesh interface engineering: Insights from bubble dynamics in electrocatalysis. *ACS Applied Materials & Interfaces*, 2021. doi:10.1021/acsami.1c07637.

[36] H. I. Lee, H.-S. Cho, M. Kim, J. Hun Lee, C. Lee, S. Lee, S.-K. Kim, C.-H. Kim, K. B. Yi, and W.-C. Cho. The structural effect of electrode mesh on hydrogen evolution reaction performance for alkaline water electrolysis. *Frontiers in Chemistry*, 9, 2021. doi:10.3389/fchem.2021.787787.

[37] E. Reyssat. Drops and bubbles in wedges. *Journal of Fluid Mechanics*, 748:641–662, 2014. doi:10.1017/jfm.2014.201.

[38] Y. Yang, J. Li, Y. Yang, L. Lan, R. Liu, Q. Fu, L. Zhang, Q. Liao, and X. Zhu. Gradient porous electrode-inducing bubble splitting for highly efficient hydrogen evolution. *Applied Energy*, 307:118278, 2022. doi:10.1016/j.apenergy.2021.118278.

[39] H. Vogt. On the gas-evolution efficiency of electrodes I - Theoretical. *Electrochimica Acta*, 56(3):1409–1416, 2011. doi:10.1016/j.electacta.2010.08.101.

[40] J. Eigeldinger and H. Vogt. The bubble coverage of gas-evolving electrodes in a flowing electrolyte. *Electrochimica Acta*, 45(27):4449–4456, 2000. ISSN 0013-4686. doi:10.1016/S0013-4686(00)00513-2.

[41] H. Vogt and K. Stephan. Local microprocesses at gas-evolving electrodes and their influence on mass transfer. *Electrochimica Acta*, 155:348–356, 2015. doi:10.1016/j.electacta.2015.01.008.

[42] H. Vogt. The quantities affecting the bubble coverage of gas-evolving electrodes. *Electrochimica Acta*, 235:495–499, 2017. doi:10.1016/j.electacta.2017.03.116.

[43] A. Bashkatov, S. S. Hossain, H. Rox, X. Yang, G. Mutschke, and K. Eckert. Dynamics of single h_2 bubbles during water electrolysis. *FC³ Fuel Cell Conference. Chemnitz, 31.05./01.06.2022*, 2022.

[44] K. Skibińska, K. Kornaus, X. Yang, D. Kutyła, M. Wojnicki, and P. Żabiński. One-step synthesis of the hydrophobic conical co-fe structures-the comparison of their active areas and electrocatalytic properties. *Electrochimica Acta*, 415:140127, 2022. doi:https://doi.org/10.1016/j.electacta.2022.140127.

[45] U. Schmidt, M. Weigert, C. Broaddus, and G. Myers. Cell detection with star-convex polygons. In *Medical Image Computing and Computer Assisted Intervention - MICCAI 2018 - 21st International Conference, Granada, Spain, September 16-20, 2018, Proceedings, Part II*, pages 265–273, 2018. doi:10.1007/978-3-030-00934-2-30.

[46] M. Weigert, U. Schmidt, R. Haase, K. Sugawara, and G. Myers. Star-convex polyhedra for 3d object detection and segmentation in microscopy. In *The IEEE Winter Conference on Applications of Computer Vision (WACV)*, 2020. doi:10.1109/WACV45572.2020.9093435.

[47] H. Hessenkemper, S. Starke, Y. Atassi, T. Ziegenhein, and D. Lucas. Bubble identification from images with machine learning methods. *International Journal of Multiphase Flow*, 155:104169, 2022. doi:10.1016/j.ijmultiphaseflow.2022.104169.

[48] D. B. Allan, T. Caswell, N. C. Keim, C. M. van der Wel, and R. W. Verweij. soft-matter/trackpy: Trackpy v0.5.0. *Zenodo*, 2021. doi:10.5281/zenodo.4682814.

[49] Z. Wang, A. C. Bovik, H. R. Sheikh, and E. P. Simoncelli. Image quality assessment: from error visibility to structural similarity. *IEEE transactions on image processing*, 13(4):600–612, 2004. doi:10.1109/TIP.2003.819861.

[50] Z. Wang and A. C. Bovik. Mean squared error: Love it or leave it? a new look at signal fidelity measures. *IEEE signal processing magazine*, 26(1): 98–117, 2009. doi:10.1109/MSP.2008.930649.

[51] R. Baumann, T. Rauscher, C. I. Bernäcker, C. Zwahr, T. Weißgärber, L. Röntzsch, and A. F. Lasagni. Laser structuring of open cell metal foams for micro scale surface enlargement. *Journal of Laser Micro/Nanoengineering*, 2020. doi:10.2961/jlmn.2020.02.2010.

[52] Y. Luo, L. Tang, U. Khan, Q. Yu, H.-M. Cheng, X. Zou, and B. Liu. Morphology and surface chemistry engineering toward pH-universal catalysts for hydrogen evolution at high current density. *Nature Communications*, 10(1), 2019. doi:10.1038/s41467-018-07792-9.

[53] D. Zhang and K. Zeng. Evaluating the behavior of electrolytic gas bubbles and their effect on the cell voltage in alkaline water electrolysis. *Industrial & Engineering Chemistry Research*, 51(42):13825–13832, 2012. doi:10.1021/ie301029e.

[54] R. Iwata, L. Zhang, K. L. Wilke, S. Gong, M. He, B. M. Gallant, and E. N. Wang. Bubble growth and departure modes on wettable/non-wettable porous foams in alkaline water splitting. *Joule*, 2021. doi:10.1016/j.joule.2021.02.015.